ACS APPLIED MATERIALS & INTERFACES

Research Article

Cite This: ACS Appl. Mater. Interfaces 2019, 11, 10697−10706

www.acsami.org

Molybdenum Trioxide (α-MoO_3) Nanoribbons for Ultrasensitive Ammonia (NH_3) Gas Detection: Integrated Experimental and Density Functional Theory Simulation Studies

Dongwook Kwak,[†,‡] Mengjing Wang,[§] Kristie J. Koski,[§] Liang Zhang,[∥] Henry Sokol,[∥] Radenka Maric,[‡,∥] and Yu Lei*[,∥]

[†]Institute of Materials Science, University of Connecticut, 97 North Eagleville Road, Storrs, Connecticut 06269, United States

[‡]Center for Clean Energy Engineering, 44 Weaver Road, Storrs, Connecticut 06269, United States

[§]Department of Chemistry, University of California, Davis, California 95616, United States

[∥]Department of Chemical and Biomolecular Engineering, University of Connecticut, 191 Auditorium Road, Storrs, Connecticut 06269, United States

Supporting Information

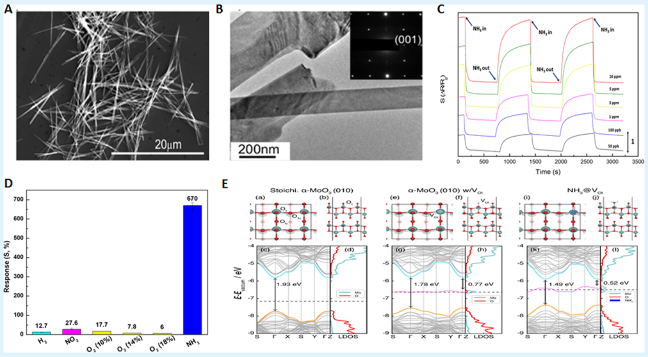

ABSTRACT: A highly-sensitive ammonia (NH_3) gas sensor based on molybdenum trioxide nanoribbons was developed in this study. α-MoO_3 nanoribbons (MoO_3 NRs) were successfully synthesized via a hydrothermal method and systematically characterized using various advanced technologies. Following a simple drop-cast process, a high-performance chemiresistive NH_3 sensor was fabricated through the deposition of a MoO_3 NR sensing film onto Au interdigitated electrodes. At an optimal operation temperature of 450 °C, the MoO_3 nanoribbon-based sensor exhibited an excellent sensitivity (0.72) at NH_3 concentration as low as 50 ppb, a fast response time of 21 s, good stability and reproducibility, and impressive selectivity against the interfering gases such as H_2, NO_2, and O_2. More importantly, the sensor represents a remarkable limit of detection of 280 ppt (calculated based on a signal-to-noise ratio of 3), which makes the as-prepared MoO_3 NR sensor the most sensitive NH_3 sensor in the literature. Moreover, density functional theory (DFT) simulations were employed to understand the adsorption energetics and electronic structures and thus shed light on the fundamentals of sensing performance. The enhanced sensitivity for NH_3 is explicitly discussed and explained by the remarkable band structure modification because of the NH_3 adsorption at the oxygen vacancy site on α-MoO_3 nanoribbons. These results verify that hydrothermally grown MoO_3 nanoribbons are a promising sensing material for enhanced NH_3 gas monitoring.

KEYWORDS: *MoO_3 nanoribbons, hydrothermal method, chemiresistive, ammonia, gas sensor, DFT simulation*

1. INTRODUCTION

Ammonia (NH_3) is one of the most common chemicals produced and used in various fields around the world.[1−3] Every year, about 2.1 to 8.1 Tg of NH_3 is emitted into the atmosphere through human activities.[2] As the industrial utilization and/or production of NH_3 have continuously grown, concerns related to human respiratory health have been rising because inhaling more than the natural level of NH_3 (sub-ppb) in the atmosphere can give rise to life-threatening maladies.[4,5] In addition to causing issues to the human respiratory system, overexposure to NH_3 can also trigger serious diseases of the skin, eyes, and lungs because of its high toxicity.[2] According to Occupational Safety and Health Administration (OSHA), the exposure time to NH_3 should be restricted to 8 h and 10 min for 25 and 35 ppm, respectively, in the workplace;[6] however, not only does the workplace necessitate accurate NH_3 monitoring but also many other fields, such as NH_3 production plants, fertilizer factories, and food process industry, demand sensitive, fast, and real-time NH_3 gas detection to counteract the accidental threats[7,8] with some of them requiring the detection at a high-temperature environment. Consequently, there is an urgent demand to develop ultrasensitive NH_3 sensors.

In the past decade, numerous gas sensing techniques have been developed for NH_3 detection in environment, utilizing metal oxides, laser spectroscopy, conducting polymers, surface acoustic waves and catalytic materials.[9] Among these gas sensing techniques, metal oxide-based sensors have attracted

Received: November 21, 2018
Accepted: February 22, 2019
Published: March 11, 2019

DOI: 10.1021/acsami.8b20502

immense attention in the gas sensing field because of its simple configuration, high sensor response, low cost and flexibility in fabrication, and capability of real-time measurement.[10−12] Basically, as a gas sensing material, metal oxides are classified into n-type and p-type semiconducting metal oxides, and most of them represent their promising electrical properties in the temperature range between 250 and 550 °C;[13] however, the p-type semiconducting metal oxides have been less selected because of their inferior gas sensing response characteristic to that of n-type ones. The gas response relation between these two types of metal oxide is represented in eq 1[14]

$$S_p = \sqrt{S_n} \qquad (1)$$

where S_n and S_p denote the gas sensing response of n-type and p-type semiconducting metal oxides, respectively. For NH_3 gas detection, metal oxides containing WO_3, SnO_2, ITO, TiO_2, ZnO, V_2O_5, and MoO_3 have been generally utilized in both research and industry fields.[15,16]

Especially, molybdenum trioxide (MoO_3) is an n-type semiconducting material with a relatively wide band gap of 3.1 eV and has been applied in various fields such as selective catalytic reduction (SCR) systems, lithium secondary batteries, electrochromic and photochromic devices and gas sensors.[17] Regarding the structure of MoO_3, there are three common crystalline phases (α, β, and hexagonal). Among those phases, the α-phase (orthorhombic) MoO_3 comprising double layers of MoO_6 octahedral bonded covalently has been mostly selected for gas sensing application because of its thermodynamic stability and high reactivity to some reducing agents.[18,19] On the basis of its encouraging characteristics as a gas sensing material, MoO_3 could be either widely or frequently utilized in the NH_3 gas sensing application; however, there have been few studies and efforts in developing MoO_3-based NH_3 gas sensing devices with ultrahigh sensitivity.

To achieve superior sensitivity in gas detection, nanostructures including nanowires, nanorods, nanobelts, nanoribbons, and so forth have been extensively employed in the field of sensors owing to their high surface-to-volume ratios and quantum confinement effects that could improve gas sensing efficiency and photon-to-electron conversion efficiency, respectively.[20,21] Miscellaneous deposition techniques have been applied in generating nanostructured MoO_3, such as chemical vapor deposition (CVD), pulsed laser deposition (PLD), spray pyrolysis, electrochemical deposition, sol−gel, sputtering, thermal evaporation, and hydrothermal method.[22,23] Although each deposition technique has its own advantages, hydrothermal synthesis outshines others because of its easily controllable growth parameters, high yielding rate, cost effectiveness, and low fabrication temperature (60−100 °C).[24]

In this work, novel MoO_3 nanoribbons (MoO_3 NRs) were synthesized using a hydrothermal method, and a thin sensing film of MoO_3 nanoribbon was deposited onto a ceramic substrate by drop casting. The morphology of as-prepared MoO_3 NRs was characterized by scanning electron microscopy (SEM) and transmission electron microscopy (TEM). The composition and crystal structure of MoO_3 NRs were investigated in detail by energy dispersive X-ray analysis (EDX), X-ray diffraction (XRD), Raman spectroscopy, and selected area electron diffraction (SAED). At an optimal operation temperature of 450 °C, the MoO_3 nanoribbon-based sensor exhibited an excellent sensitivity, rapid response, good stability and reproducibility, and impressive selectivity toward NH_3 detection. Moreover, density functional theory (DFT) simulations were employed to understand the adsorption energetics and electronic structures and thus shed light on the fundamentals of sensing performance. The enhanced sensitivity for NH_3 is explicitly discussed and explained by the remarkable band structure modification because of the NH_3 adsorption at the oxygen vacancy site on α-MoO_3 nanoribbons. The outstanding performances from the sensing results indicate that the α-MoO_3 nanoribbons are a promising gas sensing material in the development of high-performance NH_3 detection.

2. EXPERIMENTAL SECTION

2.1. Preparation of MoO_3 Nanoribbons. Molybdenum trioxide nanoribbons were synthesized through a hydrothermal method.[25] Briefly, to prepare the precursory solution of MoO_3 nanoribbons, 0.36 g of molybdenum metal powder (Sigma-Aldrich) was added into 30 mL of deionized water with shaking. Then, 2.5 mL of 30% hydrogen peroxide (H_2O_2, Sigma-Aldrich) was added dropwise with stirring, and the reaction was kept, under stirring, at room temperature for 20 min to become a dark blue slurry. The mixture was then transferred into a 50 mL stainless steel autoclave with a Teflon liner and maintained at 180 °C for 12 h. The products were allowed to air cool to room temperature. The resultant precipitates were collected, washed with ethanol, and centrifuged at <1260 rpm three times. Lastly, the precipitates were redispersed into 30 mL of DI water so as to make the suspension for MoO_3 nanoribbon film fabrication.

2.2. Characterization Methods for MoO_3 Nanoribbons. X-ray diffraction (XRD) for characterization of the crystal structure of the as-prepared MoO_3 nanoribbons was performed with a Bruker D8 Eco Advance with a Copper Kα source (Cu Kα1 = 1.5406 Å and Kα2 = 1.5444 Å). Raman spectra, confirming the MoO_3 structure, were collected using a home-built system with a Coherent Sapphire single-frequency laser (λ = 532 nm), a Leica DMi8 inverted microscope, a Semrock dichroic and razor edge filter, a Princeton Instruments SCT320 spectrometer, and a Princeton Instrument PIXIS CCD camera. For sample preparation of powder X-ray diffraction (XRD) and Raman measurements, MoO_3 solution was drop casted onto a fused silica substrate and then dried at 110 °C for 1−2 h. Scanning electron microscopy (SEM) images using a FEI Scios operating at 20 keV were utilized to observe the surface morphology. For observing detailed morphology and determining crystallinity and chemical composition of the resulting product, transmission electron microscopy (TEM) images and selected area electron diffraction (SAED) were collected using a JEOL 2100F operating at 200 kV equipped with an energy dispersive X-ray spectrometer (EDX) from Oxford, using nickel TEM grids.

2.3. Sensor Fabrication and Testing Equipment. The as-prepared MoO_3 nanoribbon solution was further suspended in DI water to obtain a constant concentration of 5 mg/mL and applied directly onto interdigitated electrodes (IDEs) through the drop-cast method.[26] The Au-interdigitated finger electrode (15 × 15 mm) on the Al_2O_3 substrate (250 μm lines and spaces) was purchased from the Electronics Design Center at Case Western University. After drop casting, the substrate with the solution drops of MoO_3 nanoribbon was placed into an oven at 50 °C and left for 15 h to evaporate water molecules completely, thus generating a dry MoO_3 thin film to bridge IDEs.

For the measurement of I−V curves, two Ni/Cr alloy wires were attached onto each end of IDEs and connected to a CHI 600E electrochemical workstation (CH Instrument, USA) for monitoring the real-time sensing characteristics (resistance) of the device. A constant DC voltage, 1 V, was applied to the sensor circuit, and the electrical resistance was computed by employing the Ohm's law ($R = V/I$). To provide a relatively high-temperature environment (~500 °C) to the sensor, a long quartz tube furnace with a volume of 1.643 L was used to control and maintain temperatures with a gas flow system.

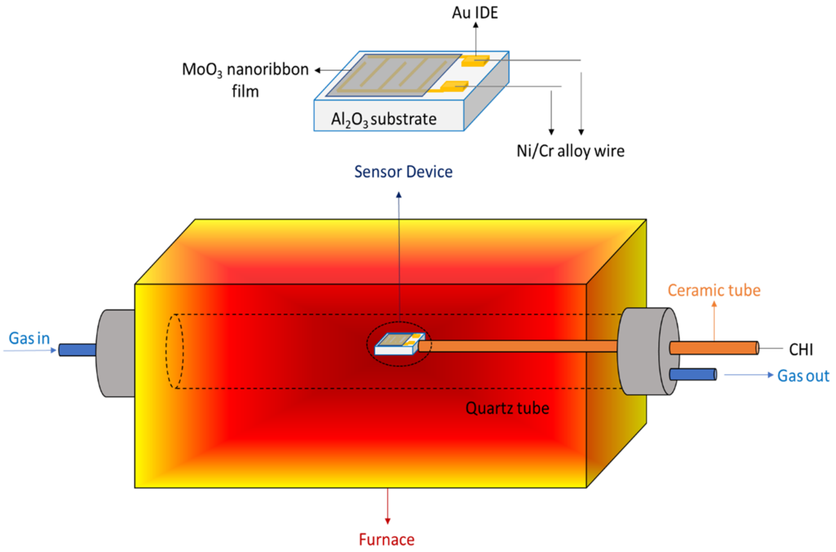

Figure 1. Schematic images of the MoO_3 nanoribbon-based sensor device (top) and the high temperature NH_3 gas sensing system (bottom).

A heating rate of 20 °C/min was applied to increase the furnace inner temperature from room temperature to 500 °C. The resistance changes during testing were measured at different concentrations of NH_3 manipulated by a Series 4040 gas dilution system (Environics, USA). Additionally, a constant gas flow rate of 1 L/min for each test was applied and achieved by the computer-controlled gas dilution system; however, because there was an inherent diluting limitation in the gas dilution system, a different gas flow rate of 2 L/min was applied to reach the lowest concentration of 50 ppb. To obtain a certain range of NH_3 concentrations from 50 ppb to 10 ppm, the zero-grade air was utilized as a carrying gas for dilution. Basically, three "on/off" cycles of NH_3 were applied for sensor signal changes in resistance, and each cycle comprises the 10 min pure air purging, followed by 10 min NH_3/air mixture purging. For other testing, a duration time for purging gases was also maintained as 10 min. The schematic images of a MoO_3 nanoribbon-based NH_3 gas sensor device and the high temperature NH_3 gas sensing system are illustrated in Figure 1.

2.4. Computational Details. All calculations were performed using the Quantum ESPRESSO[27] Package in combination with Atomic Simulation Environment (ASE)[28] based on plane-wave density functional theory (DFT).[29,30] The Bayesian error estimation exchange−correlation functional with long-range interactions functional (BEEF-vdW) has been shown to produce reliable results for interaction of molecules with layered materials[31−33] and was used to account for the van der Waals interactions. The DFT+U method with an U_{eff} = 4.5 eV was used to improve the electron localization.[34] Kohn−Sham wave functions were expanded in a plane-wave basis with a kinetic energy cutoff of 520 eV. The Monkhorst−Pack scheme was employed to sample the Brillouin zone using a 4 × 4 × 1 k-point grid for an atomic structure optimization and a 6 × 6 × 1 k-point grid for refining electronic structures.[35] Both plane wave cutoffs and k-point grid density were checked for convergence with respect to chemisorption energies. The free energy of gas molecules at 450 °C was calculated using the thermochemistry module in ASE.[28]

3. RESULTS AND DISCUSSION

3.1. Characterization Results. In general, MoO_3 has three polymorphs. Orthorhombic α-MoO_3 is the thermodynamically stable phase and thus readily synthesized as performed under the procedure in this work. Other phases of molybdenum trioxide are monoclinic β-MoO_3 and hexagonal h-MoO_3. Both of these polymorphs are known to be metastable and, in general, require more involved synthetic procedures.[36,37] The as-synthesized α-MoO_3 has a layered orthorhombic crystal structure (Figure 2a) with the space group *Pbnm*. Lattice constants of MoO_3 nanoribbons determined from XRD are *a* = 3.70 +/− 0.01 Å, *b* = 13.86 +/− 0.01 Å, and *c* = 3.96 +/− 0.01 Å (unit cell volume 203 Å^3). As-grown nanoribbons are around 10−12 nm thick with a lateral dimension of ~200 nm width by ~15 μm in length as determined by TEM (Figure 2b) and SEM (Figure 2d). Nanoribbons are a single crystal with sharp well-defined edges. Nanoribbons are drop cast onto a substrate that stack readily in a preferred orientation of (02*n*0) as shown in Figure 2c by the strong intensity of the (02*n*0) diffraction peaks. The Raman characterization of MoO_3 nanoribbons shows expected optical phonon modes (Figure 2e). EDX spectra show an elemental signal (Figure 2f) from Mo and O and no other impurities. A nickel signal in EDX is from the nickel TEM grid used to support the sample. Overall, the results shown in Figure 2 indicate the successful fabrication of high-quality α-MoO_3.

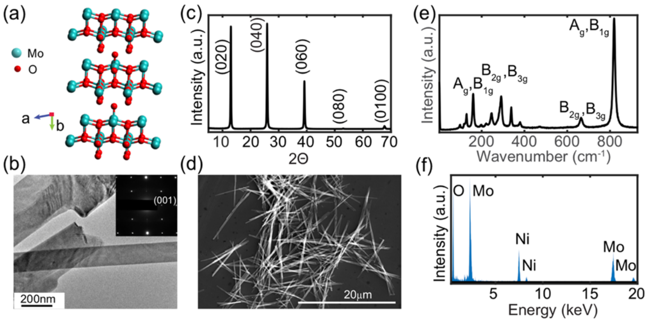

Figure 2. (a) MoO_3 nanoribbons have an orthorhombic crystal structure, (b) TEM image of MoO_3 nanoribbons with a corresponding SAED pattern shows ribbons that are single crystal in inset, (c) the powder XRD pattern of MoO_3 nanoribbons on a fused silica substrate demonstrates the preferred (02*n*0) orientation, (d) an SEM image of dried MoO_3 nanoribbons reveals a dimension of 15 μm in length, (e) Raman spectra of MoO_3 nanoribbons on the fused silica substrate with a 532 nm laser, and (f) EDX spectra of a single MoO_3 nanoribbon using TEM-EDX show only Mo and O elements in the ribbons. Nickel signals originate from the nickel TEM grid.

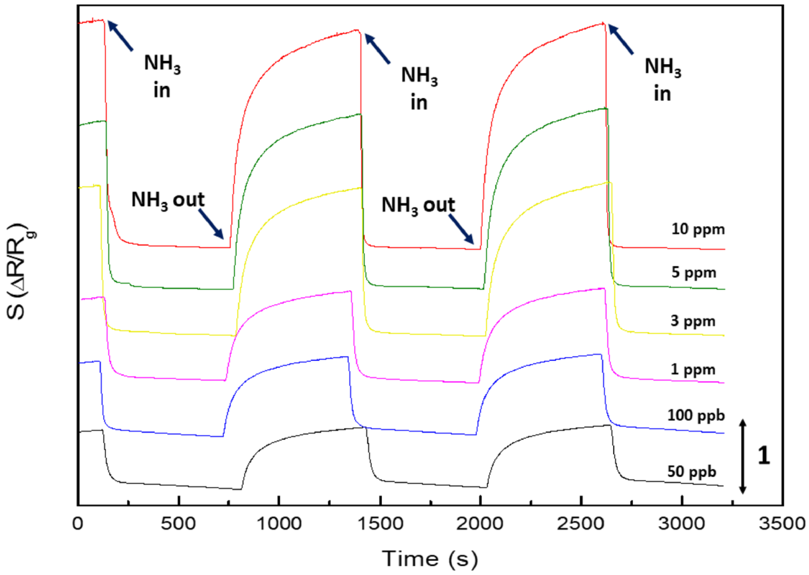

Figure 3. Typical responses of the MoO_3 nanoribbon-based sensor toward the concentration range from 50 ppb to 10 ppm NH_3 at 450 °C and a constant voltage of 1 V.

3.2. Ammonia Sensing Performance.

3.2.1. Operation Temperature. In elevated temperatures, the responses to 50 ppm NH_3 were investigated to discover the optimal operation temperature for the sensor. The relative response to NH_3 was defined as $S = \Delta R/R_g = (R_a - R_g/R_g)$, where ΔR is the difference between the resistance in air (R_a) and analyte gas (R_g).[38] Figure S1 plots the response of the sensor based on the MoO_3 nanoribbons to 50 ppm NH_3 under different temperature range from 300 to 500 °C. The sensor presents enhanced sensing responses as temperature increases; however, once the maximum sensitivity was achieved at 450 °C, the response decreased with further increase in temperature. Such typical tendency was observed in most metal oxide-based sensors,[39−43] and it might be attributed to a sintering effect on the structure of the MoO_3 nanoribbon, which can reduce the specific surface area and porosity in the nanoribbon structure, leading to a deterioration in sensitivity.[12,44] Therefore, 450 °C was chosen as the optimal operating temperature.

3.2.2. Response and Recovery Characteristics of the Developed Sensor. Figure 3 presents the variation of sensor response with NH_3 concentration ranging from 50 ppb to 10 ppm at 450 °C and an applied DC bias of 1 V. For each concentration, the sensor underwent three "on/off" cycles of NH_3 with a duration time of 10 min. The average value of sensitivity at each concentration was calculated and used to plot the calibration curve shown in Figure 4. According to Figure 4, the relationship between the sensor response and the NH_3 concentration shows a typical saturation behavior. To describe the relationship between sensitivity and gas concentration, the Freundlich isotherm model could be applied. A regressed equation of $S = 1.5141 \cdot C_{NH_3}{}^{0.2789}[\mathrm{ppm}]$ can be used to fit the experimental data with a good coefficient of $R^2 = 0.9874$.

The sensor exhibited an excellent sensitivity to all tested NH_3 concentrations even to low concentrations of NH_3 at 50 ppb ($S = 0.72$ or 72%) and 100 ppb ($S = 0.93$ or 93%). In addition to the high sensitivity, the limit of detection was estimated to be as low as 280 ppt at a signal-to-noise ratio of 3. Such high sensitivity and outstanding detection limits of our sensor can be first attributed to the high surface area of the interconnected nanoribbons. Moreover, the interaction of NH_3 with MoO_3 at the interconnecting points (on the electron transfer pathway) could significantly change the resistance of the sensor device compared to sensors made of a seamless thin film, thus being favorable for detecting a reducing gas such as NH_3.[45]

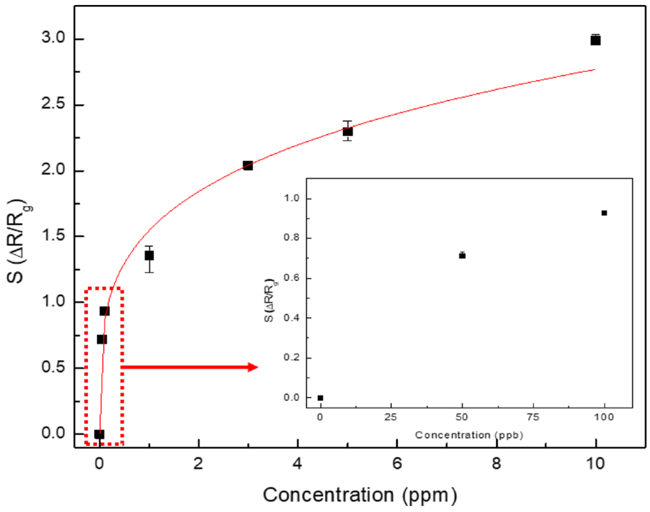

Figure 4. Calibration curve of the MoO_3 nanoribbon-based sensor for ammonia.

Because ammonia behaves as a reducing agent, the resistance of the n-type MoO_3 nanoribbon-interconnected film exposed to ammonia became lower than that in an air environment. During the three-cycle NH_3 on/off test on the sensor, the typical resistance behavior of the n-type metal oxide toward a reducing agent (NH_3) and air was obtained as shown in Figure 5a, and the sensor produced constant and reproducible responses in each cycle. Response time and recovery time are defined as the time required for the sensor resistance to reach 90% of its steady state. Figure 5b shows an enlarged single on/off cycle of NH_3 at 5 ppm (the second cycle in Figure 6a). The response and recovery times were measured

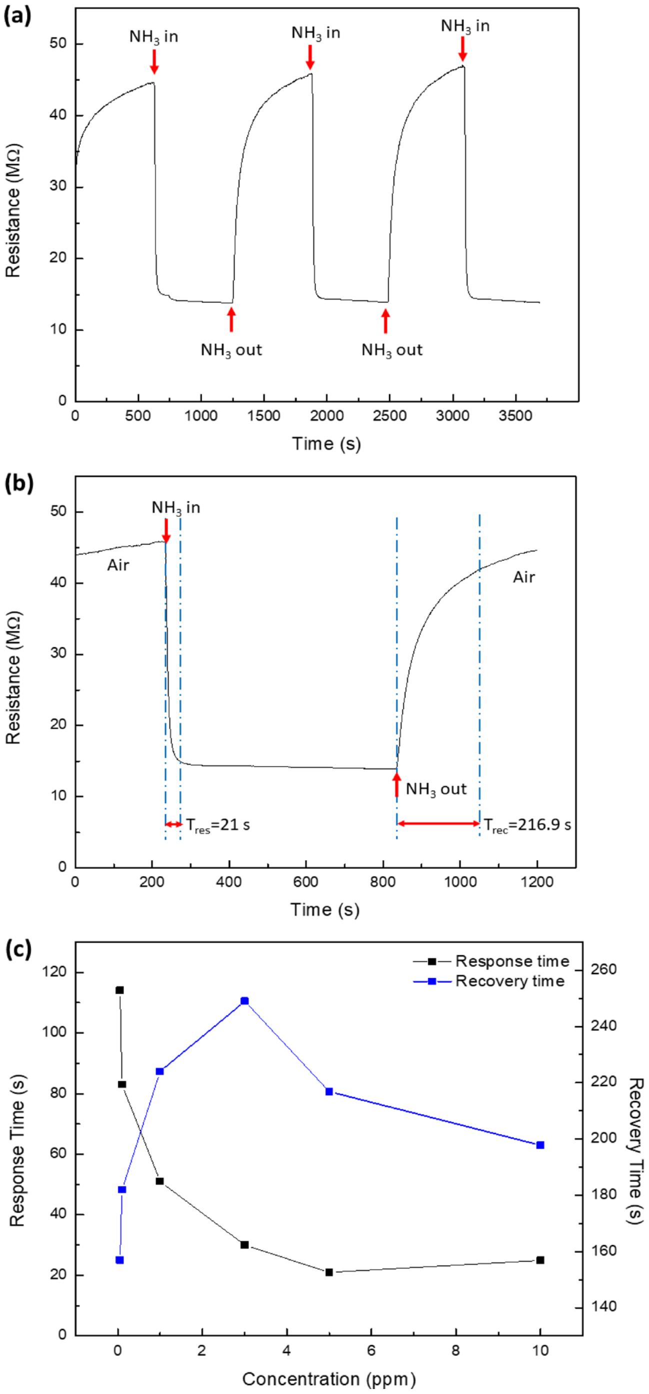

Figure 5. (a) Cyclic responses of the MoO_3 nanoribbon-based sensor toward 5 ppm ammonia, (b) the enlarged single cycle for the measurement of response and recovery times of the sensor, and (c) the response and recovery characteristics of the sensor at different NH_3 concentrations.

as 21 and 216.9 s at 5 ppm NH_3, respectively. It is noted that the response time decreases as NH_3 concentration increases, whereas the recovery time is considerably longer than the response time as represented in Figure 5c. The longer recovery time might be attributed to the fact that the absorbed oxygen ions on the surface slowly diffuse into the interfaces between the contiguous nanoribbons because of the concentration discrepancy.[46] This diffusion process is much more sluggish than the interaction between ammonia and oxygen ions that determines the response time. Consequently, the longer recovery time is expected.

3.2.3. Stability and Reproducibility of the Developed Sensor. The long-term stability of the ammonia sensing of MoO_3 nanoribbons was corroborated by consecutive cycles of NH_3 on/off at 5 ppm for 12 h. As represented in Figure 6, although a slight drift in resistance was observed over time, especially under ammonia exposure, the relatively stable signals were collected during the entire testing cycles, which can verify a good stability of the sensor. With respect to the sensor drift, a drift over time is an inevitable characteristic found in most metal oxide-based sensors in terms of long-term testing,[47] and the nature of drift has not been clearly explained yet; however, it could be attributed to the microstructural changes of the sensing film[18] during long-term testing or the testing method that applying the DC voltage might produce a leaky capacitor-type charging to the sensor, thus resulting in the drifted currents that trace the same path over time.

To study the reproducibility of the sensor, two additional sensors (sensor #2 and #3) were prepared and tested following the same procedure used for the first MoO_3 nanoribbon sensor (sensor #1). The only difference between these three sensors is that sensor #1 has been heavily used for many previous NH_3 sensing experiments, whereas sensor #2 and #3 are previously unused. Each sensor went through three cycles of 5 ppm NH_3 on/off with a 10 min duration between NH_3 and air transition. Figure S2 shows a comparison of sensitivity of the three sensors toward 5 ppm NH_3. Although the relative standard deviation (RSD) computed from the measured sensitivity of all the sensors is marginally higher (11%) than the decent value of RSD (<10%), sensor #2 and #3 are very similar in response (Figure S2). The lower response from sensor #1 may be attributed to the gradual aging of sensing materials after many times of its usage. Overall, the results indicate a considerable reproducibility of fabricated sensors.

3.2.4. Selectivity. For a gas sensor, selectivity (cross sensitivity) is the most challenging aspect toward detecting a specific gas, especially when mixed with other interfering gases.[11] To study the selectivity of our MoO_3 nanoribbon-based sensor toward NH_3, potential interferential gases such as H_2, NO_2, and O_2 were introduced at 450 °C without changing other experimental parameters. The sensing responses to those gas species and NH_3 were recorded while applying a constant voltage as 1 V. For the selectivity test, the concentrations of H_2 and NO_2 were fixed at 25 ppm that is identical to those of NH_3 and various contents (10, 14, and 18%) of O_2 modified by dilution with pure N_2 was applied. As shown in Figure 7, the sensitivity toward H_2, NO_2, and different contents of O_2 is significantly lower than that of NH_3. Tests reveal that MoO_3 sensors have a remarkably high selectivity toward NH_3.

3.2.5. Sensing Mechanism. Generally, metal oxide-based sensors in the chemiresistive configuration generate sensing signals based on the change of the surface conductivity of the sensing film. The well-defined fundamental mechanism that causes a response of metal oxides toward analyte gases is still controversial.[12] Conventionally, the depletion layer model is widely used to explain the sensing mechanism of nanostructured metal oxides.[46] When the n-type MoO_3 nanoribbon network is exposed to air, oxygen molecules are adsorbed onto the surface of the MoO_3 nanoribbons and start trapping the free electrons of the conduction band of the nanoribbons, leading to a decrease in the charge carrier density, an increment in the surface resistance, and an expanded depletion

DOI: 10.1021/acsami.8b20502
ACS Appl. Mater. Interfaces 2019, 11, 10697−10706

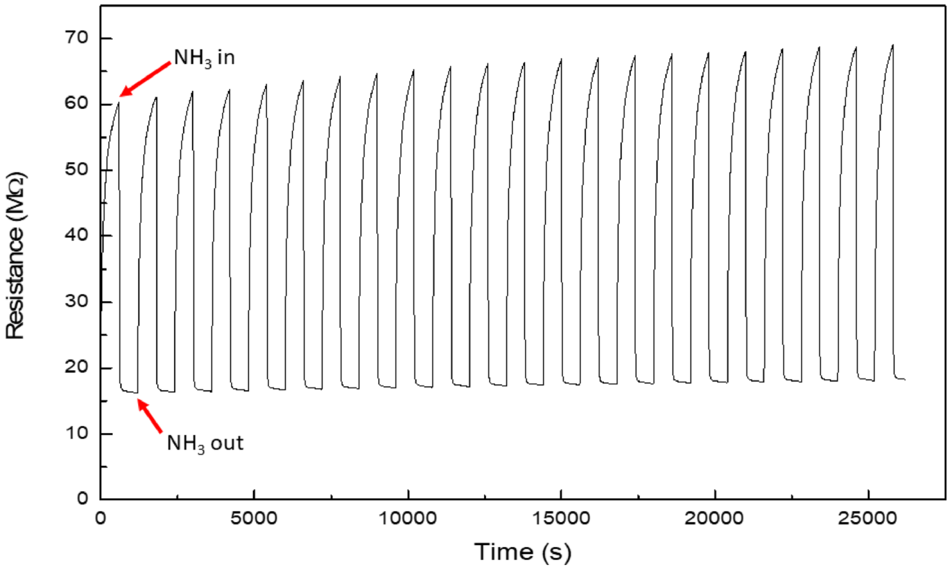

Figure 6. Long-term stability of the MoO$_3$ nanoribbon-based sensor tested for 12 h toward continuous periodic exposure to 5 ppm ammonia showing relatively good stability of the sensor.

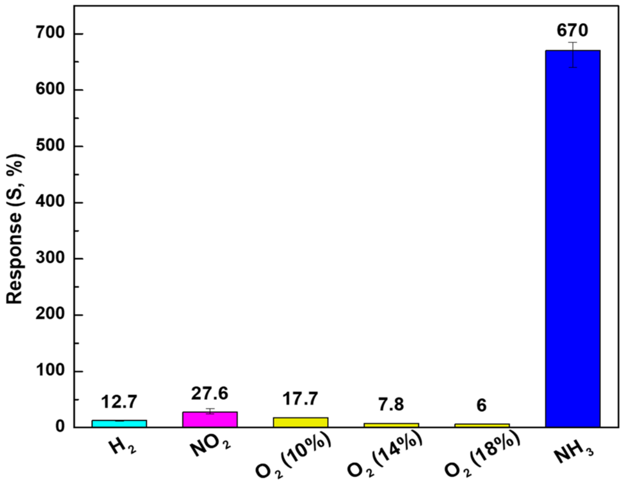

Figure 7. Sensor responses to 25 ppm H$_2$, NO$_2$, and NH$_3$ and different contents of O$_2$ at 1 V and 450 °C indicating high selectivity toward ammonia gas.

area. On the other hand, when NH$_3$ as a reducing agent is introduced to react with the oxygen ions chemisorbed on the surface of the nanoribbons, the electrons trapped by the chemisorption of oxygen are released back to the conduction band of the MoO$_3$ nanoribbons, resulting in an increase of surface conductivity, a reduction in resistance, and a shrinkage of the depletion region. In the case of exposure to air again, the oxygen molecules will be chemisorbed on the surface of nanoribbons and readily formed the large depletion region, which can be used to explain the recovery characteristic of the MoO$_3$ nanoribbons. The depletion layer model provides a qualitative and macroscopic description of the change in the charge carrier density because of the interaction between analyte gases and α-MoO$_3$ surface. However, this model is insufficient to explain the response difference between H$_2$ and NH$_3$ because they are both reducing gases that able to release the trapped electrons back to the conduction band.

To gain a further insight into the sensor mechanism at the atomistic scale, density functional theory simulations with the Hubbard U and van der Waals corrections were employed to understand the adsorption of gas molecules on the α-MoO$_3$ (010) surface and the corresponding alterations in electronic structures. The corresponding simulation results are presented in Figure 8 and Figures S3 and S4. The DFT+U calculated stoichiometric α-MoO$_3$ has a band gap of 2.01 eV in the bulk form. The band gap is slightly reduced to 1.93 eV with the cleavage of the (010) surface. These band gaps are around 1 eV smaller than the experimental values[48−50] because of the well-known underestimation of the band gap in DFT.[51] However, it does not change our conclusions because we focus more on the relative trends. Previous studies show that the monocoordinated terminal oxygen (O$_t$) has the lowest vacancy formation energy among all three nonequivalent lattice oxygen atoms.[52,53] In this study, the formation energy of terminal oxygen vacancy (V$_{Ot}$) is calculated to be 2.63 eV in the bulk of the material and 2.54 eV on the (010) surface. Thus, a higher oxygen vacancy concentration is excepted on the (010) surface than that in the bulk. Considering the fact that gas diffusion is much faster on the surface than that in the bulk, the following discussions are mainly centered on the (010) surface. NH$_3$ adsorption on the (010) α-MoO$_3$ surface is simulated on the stoichiometric surface and the one with V$_{Ot}$. When adsorbed onto the stoichiometric surface, NH$_3$ binds to the previously saturated Mo atoms with a tilting angle of 36.1°. The repulsion between the adsorbed NH$_3$ and the O$_t$ leads to a weak adsorption energy of 1.87 eV. However, a significantly stronger affinity of −1.56 eV was found between NH$_3$ and terminal oxygen vacancy, where NH$_3$ vertically adsorbs on top of the Mo atom. The large difference in adsorption energy indicates that NH$_3$ is preferentially captured at the V$_{Ot}$ position.

Figure 8a−l shows top views, side views, band structures, and local density of states (LDOS) of the α-MoO$_3$ (010) surface in the stoichiometric case, with a vacancy at the O$_t$ position, and with an NH$_3$ molecule adsorbed at the V$_{Ot}$ position. For band structures and LDOS, all energies are referenced to the vacuum level. The DFT calculated work function for the stoichiometric MoO$_3$ is 7.09 eV, which is in a reasonable agreement with the results from photoemission

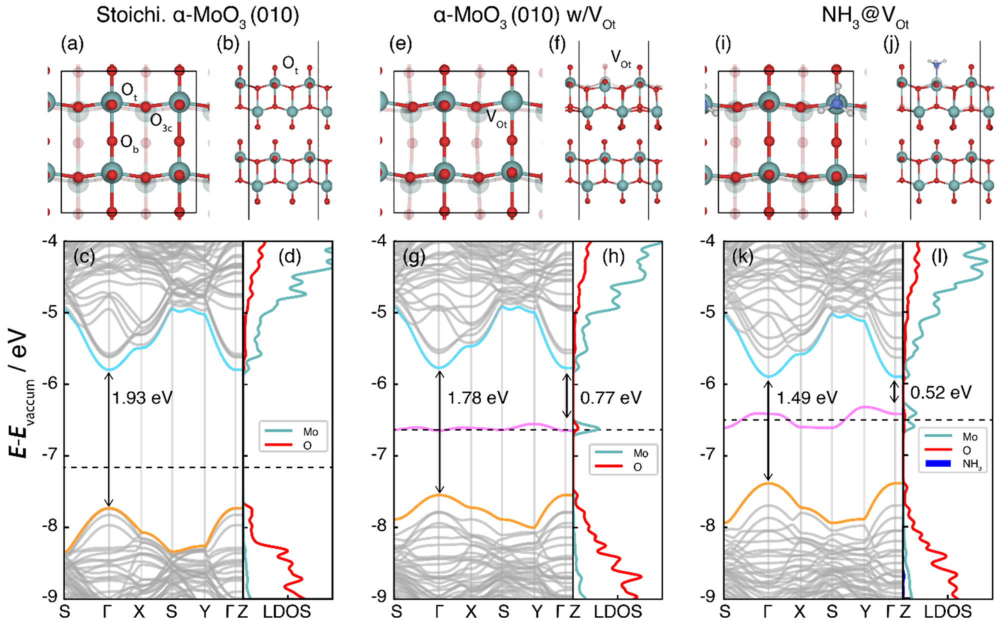

Figure 8. Atomic structures, band structures, and local density of states of the α-MoO$_3$ (010) surface (a−d) in the stoichiometric case, (e−h) with a terminal oxygen vacancy (V$_{Ot}$), and (i−l) with an NH$_3$ molecule at the V$_{Ot}$ position. For each configuration, figures on the top panel are top (left) and side (right) views of the structures. Red, grass, blue, and white balls stand for O, Mo, N, and H atoms, respectively. The three nonequivalent oxygen atoms O$_t$, O$_{3c}$, and O$_b$ of α-MoO$_3$ (010) are marked on (a). Band structures alongside the Mo and O local density of states (LDOS) are plotted in the bottom panel. The path S-Γ-X-S-Y-Γ-Z was used to compute band structures. The conduction band edge, valance band edge, and gap state are highlighted in cyan, orange, and pink, respectively. All energies are referenced to the vacuum level.

Table 1. Sensing Performance of the Recently Reported Metal Oxide-Based NH$_3$ Gas Sensors

sensing material (based/dopants)	detection limit	response time	recovery time	operation temperature	reference
SnO$_2$/In$_2$O$_3$ nanofibers	100 ppb	7 s	10 s	RT	Qi et al. (2014)[56]
nanostructured TiO$_2$	5 ppm	34 s	90 s	RT	Dhivya et al. (2014)[57]
SnO$_2$/Sr nanofibers	10 ppm	6 s		RT	Xu et al. (2015)[58]
ZnO/NiO nanocrystals	15 ppm	20 s	90 s	RT	Wang et al. (2015)[59]
nanostructured ZnO/Pd	30 ppm	198 s	334 s	200 °C	Mhlongo et al. (2015)[60]
SnO$_2$/Co$_3$O$_4$ nanospheres	5 ppm	4 s	17 s	200 °C	Wang et al. (2016)[61]
SnO$_2$/Pd/RGO nanocomposites	2 ppm	7 min	50 min	RT	Su et al. (2016)[62]
NiO/In$_2$O$_3$ *p*-*n* heterostructures	100 ppb			300 °C	Sun et al. (2016)[63]
SnO$_2$/rGO nanorods	20 ppm	8 s	13 s	RT	Chen et al. (2017)[64]
TiO$_2$/graphene nanospheres	5 ppm	114 s	304 s	RT	Ye et al. (2017)[65]
ZnO/Mn nanoparticles	20 ppm	4 s	10 s	150 °C	Sankar Ganesh et al. (2017)[66]
NiCo$_2$(OH)$_6$ nanoflakes	2 ppm	28 s	20 s	RT	Sharma et al. (2017)[67]
NiCo$_2$O$_4$ nanoflakes	2 ppm	30 s	13 s	RT	
ZnO/MoS$_2$ nanocomposite	250 ppb	10 s	11 s	RT	Zhang et al. (2017)[68]
MoO$_3$ nanosheets	500 ppb	40 s		485 °C	Jodhani et al. (2016)[22]
MoO$_3$/Si nanoparticles	400 ppb	3.6 min	7 min	400 °C	Güntner et al. (2016)[38]
MoO$_3$ nanoribbons	280 ppt	21 s	216.9 s	450 °C	this work

spectroscopy measurement (6.9 eV).[54] The valence band maximum (VBM) of the α-MoO$_3$ (010) surface has the major contribution from the O 2p states, and the conduction band minimum (CBM) is mainly composed of Mo 4d states as shown in Figure 8d, in a good agreement with previous theoretical studies. The formation of V$_{Ot}$ on the surface donates two electrons to the Mo 4d states and consequently introduces a gap state (pink band) into the vicinity of the band gap (Figure 8g). The oxygen-deficient surface has its Fermi level pinned by the gap state. At a finite temperature, electrons from the gap state can thermally populate CB with a relatively smaller gap (0.88 eV) to overcome with respect to the stoichiometric surface, contributing to a higher carrier density and an enhanced electrical conductivity.[55] Adsorption of NH$_3$ on the V$_{Ot}$ position preserves the gap state with an increased band dispersion and a substantial boarding of the state as shown in Figure 8k,l. Another important effect of the NH$_3$ adsorption is the narrowing of the band gap from 1.93 eV for the stoichiometric surface to 1.49 eV with both CBM and VBM shifting toward the Fermi level. Meanwhile, the energy gap between CBM and gap state is also further reduced to 0.52 eV. All of the above electronic structure perturbations brought on by the NH$_3$ adsorption on the V$_{Ot}$ position essentially further increase the charge carrier density at the conduction band. Thus, a more pronounced enhancement in conductivity is observed when NH$_3$ is present in the analyte gases, which gives rise to the remarkable sensitivity of α-MoO$_3$ toward NH$_3$, in a good agreement with experimental results.

DOI: 10.1021/acsami.8b20502
ACS Appl. Mater. Interfaces 2019, 11, 10697−10706

The superior selectivity of α-MoO_3 toward NH_3 against interferential gases can also be explained by their adsorption thermodynamics. We have shown in the above analysis that the oxygen vacancy and the induced gap state play the most critical role in determining the conductivity of α-MoO_3. When exposed to O_2, oxygen vacancies of α-MoO_3 are readily refilled. The higher the O_2 content, the less oxygen vacancies remained on the surface and thus, the lower the conductivity. For H_2 and NO_2, the free energies of adsorption on the V_{Ot} position are calculated to be 1.24 and 0.74 eV at 450 °C and 25 ppm. Notably, we also found that the dissociation of NO_2 at the V_{Ot} position is exergonic (−1.38 eV), leaving O filling the vacancy and NO in the gas phase. Therefore, the adsorption of H_2 and NO_2 on the V_{Ot} position is thermodynamically unfavorable, resulting in insignificant responses in sensor conductivity. Such simulation results were corroborated by the experimental observation.

Our analysis can also help to understand the effect of operating temperature on the sensor responses (Figure S1). The increase of temperature facilitates the formation of oxygen vacancies and thus creates more sites for the NH_3 adsorption. However, when the temperature is too high, the entropy term becomes dominant and turns the adsorption of NH_3 into an unfavorable process. The volcano-shaped correlation between the sensor response toward NH_3 and the operating temperature is thus a consequence of the trade-off between these two effects.

3.3. Performance Comparison to Other Metal Oxide-Based NH_3 Gas Sensors. The sensing performances of our MoO_3 nanoribbon-based sensor compared with the recently reported metal oxide-based NH_3 gas sensors are listed in Table 1. With respect to the enhanced NH_3 gas detection, a great number of recent works have adopted the hybridization with other dopants such as noble metals, carbon nanomaterials, and other metal oxides, to improve the NH_3 gas sensing performance. Although our sensing film is composed of a single metal oxide (α-MoO_3), the detection limit of our sensor is remarkably superior to that of other metal oxide-based NH_3 sensors and, from the literature study, there is no report of metal oxide-based NH_3 gas sensors that are able to achieve the sub-ppb level of NH_3 detection, especially with a single metal oxide composition; however, a relatively high operation temperature (450 °C) is required for our MoO_3 nanoribbon-based sensor, which may favor high temperature gas sensing but may consume more energy for the sensing at room temperature due to the need of heating. One potentially practical strategy to lower the operating temperature is to introduce metal doping into the MoO_3 nanoribbons. Because doping of highly active metals into metal oxides can lead to an increase in electrical conductivity and decrease in activation energy of the metal oxides, thus lowering the operation temperature of our device.

4. CONCLUSIONS

In summary, MoO_3 nanoribbons were successfully fabricated by a hydrothermal method for enhanced NH_3 gas detection. At the optimal operation temperature of 450 °C, a wide range of NH_3 concentrations (50 ppb−10 ppm) was applied to study the sensor sensitivity, and the response and recovery times. The developed sensor exhibits an outstanding sensitivity even to a very low NH_3 concentration (e.g., 50 ppb) and a relatively fast response time of 21 s. Additionally, an ultralow limit of detection (280 ppt) was achieved based on a signal-to-noise ratio of 3. During the long-term stability test, the stable sensing responses toward 5 ppm NH_3 were observed for 12 h consecutive operation. The sensor also represents an excellent selectivity against the interferential gases such as H_2, NO_2, and O_2. All experimental results are in good agreement with density functional theory simulations with the Hubbard U and van der Waals corrections, which were employed to understand the adsorption of gas molecules on the α-MoO_3(010) surface and the corresponding alternations in electronic structures. On the basis of these observed results, it can be concluded that the orthorhombic MoO_3 nanoribbon is a promising sensing material for the enhanced NH_3 gas sensing.

ASSOCIATED CONTENT

Supporting Information

The Supporting Information is available free of charge on the ACS Publications website at DOI: 10.1021/acsami.8b20502.

> The effect of operating temperature on the sensor response, the comparison of the sensitivity of three duplicate sensor units, the simulation results for the adsorption of gas molecules on the α-MoO_3 (010) surface and the corresponding alternations in electronic structures, and entropy and enthalpy corrections used for free energy calculations (PDF)

AUTHOR INFORMATION

Corresponding Author

*E-mail: yu.lei@uconn.edu. Tel.: +1-860-486-4554. Fax: +1-860-486-2959.

ORCID

Kristie J. Koski: 0000-0002-5250-2593

Notes

The authors declare no competing financial interest.

ACKNOWLEDGMENTS

We thank the financial support from DOE (DE-FE-0026219). LZ and HS thank the use of the computer time allocation at Extreme Science and Engineering Discovery Environment (XSEDE) supported through National Science Foundation under Award Number CHE160084.

REFERENCES

(1) Giddey, S.; Badwal, S. P. S.; Kulkarni, A. Review of Electrochemical Ammonia Production Technologies and Materials. *Int. J. Hydrogen Energy* **2013**, *38*, 14576−14594.

(2) Timmer, B.; Olthuis, W.; van den Berg, A. Ammonia Sensors and Their Applications - A Review. *Sens. Actuators, B* **2005**, *107*, 666−677.

(3) Mani, G. K.; Rayappan, J. B. B. Selective Detection of Ammonia Using Spray Pyrolysis Deposited Pure and Nickel Doped ZnO Thin Films. *Appl. Surf. Sci.* **2014**, *311*, 405−412.

(4) Ghosh, S. P.; Das, K. C.; Tripathy, N.; Bose, G.; Kim, D. H.; Lee, T.; Myoung, J. M.; Kar, J. P. Ammonia Sensing Behavior of Zinc Oxide Thin Films and Nanostructures. *IUP J. Electr. Electron. Eng.* **2016**, *9*, 78−84.

(5) Talwar, V.; Singh, O.; Singh, R. C. ZnO Assisted Polyaniline Nanofibers and Its Application as Ammonia Gas Sensor. *Sens. Actuators, B* **2014**, *191*, 276−282.

(6) Mani, G. K.; Rayappan, J. B. B. A Highly Selective and Wide Range Ammonia Sensor - Nanostructured ZnO:Co Thin Film. *Mater. Sci. Eng. B* **2015**, *191*, 41−50.

(7) Tabrizi, L.; Chiniforoshan, H. High-Performance Room Temperature Gas Sensor Based on Gold(III) Pincer Complex with High Sensitivity for NH_3. *Sens. Actuators, B* **2017**, *245*, 815−820.

(8) Huang, J.; Wang, J.; Gu, C.; Yu, K.; Meng, F.; Liu, J. A Novel Highly Sensitive Gas Ionization Sensor for Ammonia Detection. *Sens. Actuators, A* **2009**, *150*, 218−223.
(9) Pandeeswari, R.; Jeyaprakash, B. G. Nanostructured α-MoO_3 thin Film as a Highly Selective TMA Sensor. *Biosens. Bioelectron.* **2014**, *53*, 182−186.
(10) Zakrzewska, K. Mixed Oxides as Gas Sensors. *Thin Solid Films* **2001**, *391*, 229−238.
(11) Barsan, N.; Koziej, D.; Weimar, U. Metal Oxide-Based Gas Sensor Research: How To? *Sens. Actuators, B* **2007**, *121*, 18−35.
(12) Wang, C.; Yin, L.; Zhang, L.; Xiang, D.; Gao, R. Metal Oxide Gas Sensors: Sensitivity and Influencing Factors. *Sensors* **2010**, *10*, 2088−2106.
(13) Franke, M. E.; Koplin, T. J.; Simon, U. Metal and Metal Oxide Nanoparticles in Chemiresistors: Does the Nanoscale Matter? *Small* **2006**, *2*, 36−50.
(14) Kim, H.-J.; Lee, J.-H. Highly Sensitive and Selective Gas Sensors Using p-Type Oxide Semiconductors: Overview. *Sens. Actuators, B* **2014**, *192*, 607−627.
(15) Shahabuddin, M.; Sharma, A.; Kumar, J.; Tomar, M.; Umar, A.; Gupta, V. Metal Clusters Activated SnO_2 Thin Film for Low Level Detection of NH_3 Gas. *Sens. Actuators, B* **2014**, *194*, 410−418.
(16) Shankar, P.; Rayappan, J. B. B. Gas Sensing Mechanism of Metal Oxides: The Role of Ambient Atmosphere , Type of Semiconductor and Gases - A Review. *Sci. Jet* **2015**, *4*, 1−18.
(17) Uthanna, S.; Nirupama, V.; Pierson, J. F. Substrate Temperature Influenced Structural, Electrical and Optical Properties of Dc Magnetron Sputtered MoO_3 Films. *Appl. Surf. Sci.* **2010**, *256*, 3133−3137.
(18) Prasad, A. K.; Gouma, P. I.; Kubinski, D. J.; Visser, J. H.; Soltis, R. E.; Schmitz, P. J. Reactively Sputtered MoO_3 Films for Ammonia Sensing. *Thin Solid Films* **2003**, *436*, 46−51.
(19) Pachlhofer, J. M.; Jachs, C.; Franz, R.; Franzke, E.; Köstenbauer, H.; Winkler, J.; Mitterer, C. Structure Evolution in Reactively Sputtered Molybdenum Oxide Thin Films. *Vaccum* **2016**, *131*, 246−251.
(20) Li, Q.; Kumar, V.; Li, Y.; Zhang, H.; Marks, T. J.; Chang, R. P. H. Fabrication of ZnO Nanorods and Nanotubes in Aqueous Solutions. *Chem. Mater.* **2005**, *17*, 1001−1006.
(21) Kemmler, J. A.; Pokhrel, S.; Mädler, L.; Weimar, U.; Barsan, N. Flame Spray Pyrolysis for Sensing at the Nanoscale. *Nanotechnology* **2013**, *24*, 442001.
(22) Jodhani, G.; Huang, J.; Gouma, P. Flame Spray Synthesis and Ammonia Sensing Properties of Pure-MoO_3 Nanosheets. *J. Nanotechnol.* **2016**, *2016*, 1−5.
(23) Qiu, Y.; Yang, M.; Fan, H.; Xu, Y.; Shao, Y.; Yang, X.; Yang, S. Synthesis of ZnO Nanorod Arrays on Zn Substrates by a Gas-Solution-Solid Method and Their Application as an Ammonia Sensor. *J. Mater. Sci.* **2014**, *49*, 347−352.
(24) Shaziman, S.; Ismail@rosdi, A. S.; Mamat, M. H.; Zoolfakar, A. S. Influence of Growth Time and Temperature on the Morphology of ZnO Nanorods via Hydrothermal. *IOP Conf. Ser. Mater. Sci. Eng.* **2015**, *99*, No. 012016.
(25) Li, G.; Jiang, L.; Pang, S.; Peng, H.; Zhang, Z. Molybdenum Trioxide Nanostructures: The Evolution from Helical Nanosheets to Crosslike Nanoflowers to Nanobelts. *J. Phys. Chem. B* **2006**, *110*, 24472−24475.
(26) Liu, Y.; Lei, Y. Pt-CeO_2 Nanofibers Based High-Frequency Impedancemetric Gas Sensor for Selective CO and C_3H_8 Detection in High-Temperature Harsh Environment. *Sens. Actuators, B* **2013**, *188*, 1141−1147.
(27) Giannozzi, P.; Baroni, S.; Bonini, N.; Calandra, M.; Car, R.; Cavazzoni, C.; Ceresoli, D.; Chiarotti, G. L.; Cococcioni, M.; Dabo, I.; Corso, A. D.; de Gironcoli, S.; Fabris, S.; Fratesi, G.; Gebauer, R.; Gerstmann, U.; Gougoussis, C.; Kokalj, A.; Lazzeri, M.; Martin-Samos, L.; Marzari, N.; Mauri, F.; Mazzarello, R.; Paolini, S.; Pasquarello, A.; Paulatto, L.; Sbraccia, C.; Scandolo, S.; Sclauzero, G.; Seitsonen, A. P.; Smogunov, A.; Umari, P.; Wentzcovitch, R. M. QUANTUM ESPRESSO: A Modular and Open-Source Software Project for Quantum Simulations of Materials. *J. Phys. Condens. Matter* **2009**, *21*, 395502.
(28) Hjorth Larsen, A.; Mortensen, J. J.; Blomqvist, J.; Castelli, I. E.; Christensen, R.; Dułak, M.; Friis, J.; Groves, M. N.; Hammer, B.; Hargus, C.; Hermes, E. D.; Jennings, P. C.; Bjerre Jensen, P.; Kermode, J.; Kitchin, J. R.; Leonhard Kolsbjerg, E.; Kubal, J.; Kaasbjerg, K.; Lysgaard, S.; Bergmann Maronsson, J.; Maxson, T.; Olsen, T.; Pastewka, L.; Peterson, A.; Rostgaard, C.; Schiøtz, J.; Schütt, O.; Strange, M.; Thygesen, K. S.; Vegge, T.; Vilhelmsen, L.; Walter, M.; Zeng, Z.; Jacobsen, K. W. The Atomic Simulation Environment - A Python Library for Working with Atoms. *J. Phys.: Condens. Matter* **2017**, *29*, 273002.
(29) Hohenberg, P.; Kohn, W. Inhomogeneous Electron Gas. *Phys. Rev.* **1964**, *136*, B864−B871.
(30) Kohn, W.; Sham, L. J. Self-Consistent Equations Including Exchange and Correlation Effects. *Phys. Rev.* **1965**, *140*, A1133−A1138.
(31) Li, H.; Tsai, C.; Koh, A. L.; Cai, L.; Contryman, A. W.; Fragapane, A. H.; Zhao, J.; Han, H. S.; Manoharan, H. C.; Abild-Pedersen, F.; Norskov, J. K.; Zheng, X. Activating and Optimizing MoS_2 basal Planes for Hydrogen Evolution through the Formation of Strained Sulphur Vacancies. *Nat. Mater.* **2016**, *15*, 48−53.
(32) Tsai, C.; Chan, K.; Abild-Pedersen, F.; Nørskov, J. K. Active Edge Sites in $MoSe_2$ and WSe_2 catalysts for the Hydrogen Evolution Reaction: A Density Functional Study. *Phys. Chem. Chem. Phys.* **2014**, *16*, 13156−13164.
(33) Tsai, C.; Chan, K.; Nørskov, J. K.; Abild-Pedersen, F. Theoretical Insights into the Hydrogen Evolution Activity of Layered Transition Metal Dichalcogenides. *Surf. Sci.* **2015**, *640*, 133−140.
(34) Dudarev, S. L.; Botton, G. A.; Savrasov, S. Y.; Humphreys, C. J.; Sutton, A. P. Electron Energy Loss Spectra and the Structural Stability of Nickel Oxide An LSDA U Study. *Phys. Rev. B* **1998**, *57*, 1505−1509.
(35) Monkhorst, H. J.; Pack, J. D. Special Points for Brillouin-Zone Integrations. *Phys. Rev. B* **1976**, *13*, 5188−5192.
(36) McCarron, E. M., III β-MoO_3: A Metastable Analogue of WO_3. *J. Chem. Soc., Chem. Commun.* **1986**, *101*, 336−338.
(37) Muraoka, Y.; Grenier, J. C.; Petit, S.; Pouchard, M. Preparation of Hexagonal MoO_3 by "Chimie Douce" Reaction with NO_2. *Solid State Sci.* **1999**, *1*, 133−148.
(38) Güntner, A. T.; Righettoni, M.; Pratsinis, S. E. Selective Sensing of NH_3 by Si-Doped α-MoO_3 for Breath Analysis. *Sens. Actuators, B* **2016**, *223*, 266−273.
(39) Jing, Z.; Zhan, J. Fabrication and Gas-Sensing Properties of Porous ZnO Nanoplates. *Adv. Mater.* **2008**, *20*, 4547−4551.
(40) Malyshev, V. V.; Pislyakov, A. V. Investigation of Gas-Sensitivity of Sensor Structures to Hydrogen in a Wide Range of Temperature, Concentration and Humidity of Gas Medium. *Sens. Actuators, B* **2008**, *134*, 913−921.
(41) Kim, I.-D.; Rothschild, A.; Lee, B. H.; Kim, D. Y.; Jo, S. M.; Tuller, H. L. Ultrasensitive Chemiresistors Based on Electrospun TiO_2 Nanofibers. *Nano Lett.* **2006**, *6*, 2009−2013.
(42) Cao, M.; Wang, Y.; Chen, T.; Antonietti, M.; Niederberger, M. A Highly Sensitive and Fast-Responding Ethanol Sensor Based on $CdIn_2O_4$ Nanocrystals Synthesized by a Nonaqueous Sol - Gel Route. *Chem. Mater.* **2008**, *20*, 5781−5786.
(43) Van Duy, N.; Van Hieu, N.; Huy, P. T.; Chien, N. D.; Thamilselvan, M.; Yi, J. Mixed SnO_2/TiO_2 included with Carbon Nanotubes for Gas-Sensing Application. *Phys. E (Amsterdam, Neth.)* **2008**, *41*, 258−263.
(44) Chiang, T.; Yeh, H. The Synthesis of α-MoO_3 by Ethylene Glycol. *Materials (Basel).* **2013**, *6*, 4609−4625.
(45) Chen, T.-Y.; Chen, H.-I.; Hsu, C.-S.; Huang, C.-C.; Wu, J.-S.; Chou, P.-C.; Liu, W.-C. Characteristics of ZnO Nanorods-Based Ammonia Gas Sensors with a Cross-Linked Configuration. *Sensors Actuators B. Chem.* **2015**, *221*, 491−498.
(46) Yang, S.; Wang, Z.; Hu, Y.; Luo, X.; Lei, J.; Zhou, D.; Fei, L.; Wang, Y.; Gu, H. Highly Responsive Room-Temperature Hydrogen

Sensing of α-MoO_3 Nanoribbon Membranes. *ACS Appl. Mater. Interfaces* **2015**, *7*, 9247−9253.

(47) Korotcenkov, G. Metal Oxides for Solid-State Gas Sensors: What Determines Our Choice? *Mater. Sci. Eng. B Solid-State Mater. Adv. Technol.* **2007**, *139*, 1−23.

(48) Carcia, P. F.; McCarron, E. M., III Synthesis and Properties of Thin Film Polymorphs of Molybdenum Trioxide. *Thin Solid Films* **1987**, *155*, 53−63.

(49) Bouzidi, A.; Benramdane, N.; Tabet-Derraz, H.; Mathieu, C.; Khelifa, B.; DesFeux, R. Effect of Substrate Temperature on the Structural and Optical Properties of MoO_3 Thin Films Prepared by Spray Pyrolysis Technique. *Mater. Sci. Eng. B* **2003**, *97*, 5−8.

(50) Kröger, M.; Hamwi, S.; Meyer, J.; Riedl, T.; Kowalsky, W.; Kahn, A. P-Type Doping of Organic Wide Band Gap Materials by Transition Metal Oxides: A Case-Study on Molybdenum Trioxide. *Org. Electron.* **2009**, *10*, 932−938.

(51) Perdew, J. P. Density Functional Theory and the Band Gap Problem. *Int. J. Quantum Chem.* **1985**, *28*, 497−523.

(52) Rellán-Piñeiro, M.; López, N. One Oxygen Vacancy, Two Charge States: Characterization of Reduced α-MoO_3(010) through Theoretical Methods. *J. Phys. Chem. Lett.* **2018**, *9*, 2568−2573.

(53) Inzani, K.; Grande, T.; Vullum-Bruer, F.; Selbach, S. M. A van Der Waals Density Functional Study of MoO_3 and Its Oxygen Vacancies. *J. Phys. Chem. C* **2016**, *120*, 8959−8968.

(54) Greiner, M. T.; Chai, L.; Helander, M. G.; Tang, W. M.; Lu, Z. H. Transition Metal Oxide Work Functions: The Influence of Cation Oxidation State and Oxygen Vacancies. *Adv. Funct. Mater.* **2012**, *22*, 4557−4568.

(55) Ashcroft, N. W.; Mermin, N. D. *Solid State Physics*; Holt, Rinehart and Winston: New York, 1976.

(56) Qi, Q.; Wang, P.-P.; Zhao, J.; Feng, L.-L.; Zhou, L.-J.; Xuan, R.-F.; Liu, Y.-P.; Li, G.-D. SnO_2 Nanoparticle-Coated In_2O_3 Nanofibers with Improved NH_3 Sensing Properties. *Sens. Actuators, B* **2014**, *194*, 440−446.

(57) Dhivya, P.; Prasad, A. K.; Sridharan, M. Nanostructured TiO_2 films: Enhanced NH_3 detection at Room Temperature. *Ceram. Int.* **2014**, *40*, 409−415.

(58) Xu, S.; Kan, K.; Yang, Y.; Jiang, C.; Gao, J.; Jing, L.; Shen, P.; Li, L.; Shi, K. Enhanced NH_3 Gas Sensing Performance Based on Electrospun Alkaline-Earth Metals Composited SnO_2 Nanofibers. *J. Alloys Compd.* **2015**, *618*, 240−247.

(59) Wang, J.; Yang, P.; Wei, X. High-Performance, Room-Temperature, and No-Humidity-Impact Ammonia Sensor Based on Heterogeneous Nickel Oxide and Zinc Oxide Nanocrystals. *ACS Appl. Mater. Interfaces* **2015**, *7*, 3816−3824.

(60) Mhlongo, G. H.; Motaung, D. E.; Swart, H. C. Pd^{2+} Doped ZnO Nanostructures: Structural, Luminescence and Gas Sensing Properties. *Mater. Lett.* **2015**, *160*, 200−205.

(61) Wang, L.; Lou, Z.; Zhang, R.; Zhou, T.; Deng, J.; Zhang, T. Hybrid Co_3O_4/SnO_2 Core-Shell Nanospheres as Real-Time Rapid-Response Sensors for Ammonia Gas. *ACS Appl. Mater. Interfaces* **2016**, *8*, 6539−6545.

(62) Su, P. G.; Yang, L.-Y. NH3gas Sensor Based on Pd/SnO_2/RGO Ternary Composite Operated at Room-Temperature. *Sens. Actuators, B* **2016**, *223*, 202−208.

(63) Sun, C.; Dutta, P. K. Selective Detection of Part per Billion Concentrations of Ammonia Using a p-n Semiconducting Oxide Heterostructure. *Sens. Actuators, B* **2016**, *226*, 156−169.

(64) Chen, Y.; Zhang, W.; Wu, Q. A Highly Sensitive Room-Temperature Sensing Material for NH3: SnO_2-Nanorods Coupled by RGO. *Sens. Actuators, B* **2017**, *242*, 1216−1226.

(65) Ye, Z.; Tai, H.; Guo, R.; Yuan, Z.; Liu, C.; Su, Y.; Chen, Z.; Jiang, Y. Excellent Ammonia Sensing Performance of Gas Sensor Based on Graphene/Titanium Dioxide Hybrid with Improved Morphology. *Appl. Surf. Sci.* **2017**, *419*, 84−90.

(66) Sankar Ganesh, R.; Durgadevi, E.; Navaneethan, M.; Patil, V. L.; Ponnusamy, S.; Muthamizhchelvan, C.; Kawasaki, S.; Patil, P. S.; Hayakawa, Y. Low Temperature Ammonia Gas Sensor Based on Mn-Doped ZnO Nanoparticle Decorated Microspheres. *J. Alloys Compd.* **2017**, *721*, 182−190.

(67) Sharma, A.; Bhojane, P.; Rana, A. K.; Kumar, Y.; Shirage, P. M. Mesoporous Nickel Cobalt Hydroxide/Oxide as an Excellent Room Temperature Ammonia Sensor. *Scr. Mater.* **2017**, *128*, 65−68.

(68) Zhang, D.; Jiang, C.; Sun, Y. Room-Temperature High-Performance Ammonia Gas Sensor Based on Layer-by-Layer Self-Assembled Molybdenum Disulfide/Zinc Oxide Nanocomposite Film. *J. Alloys Compd.* **2017**, *698*, 476−483.